

See discussions, stats, and author profiles for this publication at: <https://www.researchgate.net/publication/266946513>

Au-36(SPh)(24) Nanomolecules: X-ray Crystal Structure, Optical Spectroscopy, Electrochemistry, and Theoretical Analysis

ARTICLE in THE JOURNAL OF PHYSICAL CHEMISTRY B · OCTOBER 2014

Impact Factor: 3.3 · DOI: 10.1021/jp506508x · Source: PubMed

CITATIONS

8

READS

67

6 AUTHORS, INCLUDING:



Praneeth Reddy Nimmala

University of Mississippi

14 PUBLICATIONS 217 CITATIONS

[SEE PROFILE](#)



Amala Dass

University of Mississippi

108 PUBLICATIONS 3,287 CITATIONS

[SEE PROFILE](#)

Au₃₆(SPh)₂₄ Nanomolecules: X-ray Crystal Structure, Optical Spectroscopy, Electrochemistry, and Theoretical Analysis

Praneeth Reddy Nimmala,[†] Stefan Knoppe,[‡] Vijay Reddy Jupally,[†] Jared H. Delcamp,[†] Christine M. Aikens,[§] and Amala Dass*,[†]

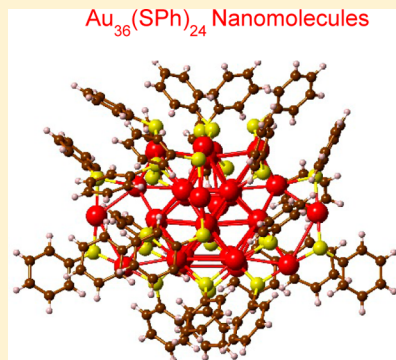
[†]Department of Chemistry and Biochemistry, University of Mississippi, Oxford, Mississippi 38677, United States

[‡]Molecular Imaging and Photonics, Department of Chemistry, KU Leuven, Celestijnenlaan 200D, 3001 Heverlee, Belgium

[§]Department of Chemistry, Kansas State University, Manhattan, Kansas 66506, United States

S Supporting Information

ABSTRACT: The physicochemical properties of gold:thiolate nanomolecules depend on their crystal structure and the capping ligands. The effects of protecting ligands on the crystal structure of the nanomolecules are of high interest in this area of research. Here we report the crystal structure of an all aromatic thiophenolate-capped Au₃₆(SPh)₂₄ nanomolecule, which has a face-centered cubic (*fcc*) core similar to other nanomolecules such as Au₃₆(SPh-tBu)₂₄ and Au₃₆(SC₅H₉)₂₄ with the same number of gold atoms and ligands. The results support the idea that a stable core remains intact even when the capping ligand is varied. We also correct our earlier assignment of “Au₃₆(SPh)₂₃” which was determined based on MALDI mass spectrometry which is more prone to fragmentation than ESI mass spectrometry. We show that ESI mass spectrometry gives the correct assignment of Au₃₆(SPh)₂₄, supporting the X-ray crystal structure. The electronic structure of the title compound was computed at different levels of theory (PBE, LDA, and LB94) using the coordinates extracted from the single crystal X-ray diffraction data. The optical and electrochemical properties were determined from experimental data using UV-vis spectroscopy, cyclic voltammetry, and differential pulse voltammetry. Au₃₆(SPh)₂₄ shows a broad electrochemical gap near 2 V, a desirable optical gap of ~1.75 eV for dye-sensitized solar cell applications, as well as appropriately positioned electrochemical potentials for many electrocatalytic reactions.



INTRODUCTION

Gold nanomolecules are ultrasmall (<2 nm) chemical entities with a fixed composition, comprising a specific number of gold atoms and protecting thiolate ligands.^{1–3} Their size-dependent optical⁴ and electrochemical⁵ properties offer potential for applications in catalysis,⁶ bioimaging,^{7,8} and drug delivery,⁹ attracting enormous attention in this research area. These nanomolecules are of the form Au_x(SR)_y (SR: thiolate) and possess distinct molecule-like properties as a result of their unique geometric and electronic structure.^{3,4,10} Single crystal X-ray crystal structures of several of these nanomolecules have been reported.¹¹ These typically have a common central Au(0) structural motif with a compact geometry, surrounded by –SR–Au–SR– and/or –SR–Au–SR–Au–SR– motifs.^{2,12,13}

Employing aliphatic ligands such as hexanethiolate or dodecanethiolate during the synthesis leads to the formation of commonly known Au:SR nanomolecules with the compositions Au₂₅(SC_nH_{2n+1})₁₈, Au₃₈(SC_nH_{2n+1})₂₄, Au₆₇(SC_nH_{2n+1})₃₅, and Au₁₄₄(SC_nH_{2n+1})₆₀.^{14–19} The most commonly employed thiolate ligand, HS–CH₂–CH₂–Ph,²⁰ also gives these 25-, 38-, 67-,¹⁷ 144-, 329-,²¹ 500-,²² and 940-Au atom²³ core sizes. Therefore, for the purposes concerned here, we group nanoparticles stabilized by the –SCH₂CH₂Ph ligand with those passivated by aliphatic ligands. The 25-, 38-, and

144-atom Au:SR clusters are the most commonly studied systems,^{24–27} which have been reproduced by various researchers worldwide and analyzed by various computational researchers.^{1,2,26–34} In this work, we focused on the Au₃₆(SR)₂₄ nanoparticle protected by the aromatic ligand –SPh. We report the total structure of this cluster from single crystal X-ray diffraction studies and give a comprehensive experimental and theoretical characterization of its properties. To the best of our knowledge, this is the first time that the total structure of any Au:SR nanocluster protected by HSPh is discovered, although crystal structures with other aromatic ligands have been reported.³⁵

The foundation for aromatic thiolate studies was established by earlier studies by the Murray and Whetten groups,^{20,36} but no distinct compositions were identified, since fragmentation-free mass spectrometry⁵ was not established then. The first crystal structure of Au₁₀₂(SC₆H₄–COOH)₄₄ by Kornberg's group also happens to contain an aromatic thiolate, with no specific comparison to aliphatic protected nanomolecules.¹²

Special Issue: Spectroscopy of Nano- and Biomaterials Symposium

Received: June 30, 2014

Revised: September 26, 2014

Published: October 15, 2014

However, there was a void in our understanding in the area of gold nanomolecules protected with organic aromatic thiolates.

$\text{Au}_{36}(\text{SPh}-\text{X})_{24}$ is a well-known molecule that has been previously isolated by researchers in this field. With respect to prior research efforts, we seek to provide a timeline to clearly frame the importance of the results in this manuscript.

(1) $\text{Au}_{36}(\text{SPh})_{24}$ was originally misassigned as “ $\text{Au}_{36}(\text{SPh})_{23}$ ” in 2011.³⁷ Two of us isolated and compositionally assigned $\text{Au}_{36}(\text{SPh})_{24}$ as an organic aromatic thiolate-stabilized molecule for the first time. In this report,³⁷ we noted that heating $\text{Au}_{67}(\text{SCH}_2\text{CH}_2\text{Ph})_{35}$ and $\text{Au}_{103-105}(\text{SCH}_2\text{CH}_2\text{Ph})_{45-46}$ in the presence of excess aromatic thiol, HSPh, yields $\text{Au}_{36}(\text{SPh})_{24}$. It was shown that the 67 and ~103–105 atom species convert to the $\text{Au}_{36}(\text{SPh})_{24}$ species through a $\text{Au}_{38}(\text{SCH}_2\text{CH}_2\text{Ph})_{14-}(\text{SPh})_{10}$ intermediate. Experimental data showed that, when the thiophenol ligand count exceeded 10 in the Au_{38} intermediate, it converted to Au_{36} . A change in core size from 38 atoms to 36 atoms was explicitly stated.

(2) In 2012, Jin and co-workers³⁸ reproduced our results showing that $\text{Au}_{36}(\text{SC}_6\text{H}_4-\text{tBu})_{24}$ can be synthesized directly from $\text{Au}_{38}(\text{SCH}_2\text{CH}_2\text{Ph})_{24}$. As expected, the effect of substituting a tBu group in the *para*-position did not alter the chemistry, and still led to the formation of Au_{36} , with an optical spectrum as reported earlier. In 2013,³⁹ the same group again reproduced our finding that when the number of 4-*tert*-butylphenylthiolate ligands reaches a threshold value (ca. 12) a structural change occurs via a proposed disproportionation process. The aromatic thiolate ligands were speculatively ascribed to having unusual characteristics beyond a simple steric involvement on stabilizing the Au core.

(3) More recently, the crystal structure of nonaromatic cyclopentanethiolate protected $\text{Au}_{36}(\text{SC}_5\text{H}_9)_{24}$ has been reported.⁴⁰ The formation of the $\text{Au}_{36}(\text{SR})_{24}$ nanomolecule with cyclopentanethiolate challenges the hypothesis that aromatic thiolate ligands are necessary for the formation of $\text{Au}_{36}(\text{SR})_{24}$. A systematic investigation on the effects of aromatic ligands versus sterically hindered aliphatic ligands is currently lacking.⁴¹⁻⁴³

In this manuscript, we provide a unifying study with full characterization on $\text{Au}_{36}(\text{SPh})_{24}$, including X-ray crystallography, mass spectrometry, optical spectroscopy, and electrochemistry.

Herein, we successfully solved the crystal structure of $\text{Au}_{36}(\text{SPh})_{24}$ using X-ray crystallography. Combined with previous reports on $\text{Au}_{36}(\text{SC}_6\text{H}_4-\text{tBu})_{24}$ and $\text{Au}_{36}(\text{SC}_5\text{H}_9)_{24}$, our work sets the first example of a Au:SR nanomolecule that has been crystallographically characterized bearing three distinct thiolate ligands (note that the $\text{Ag}_{44}(\text{SR})_{30}$ cluster has been structurally characterized with different ligands^{44,45}). In addition, we present detailed mass spectrometric assignment and fragmentation of the nanomolecule and its electrochemical and optical properties. Density functional theory (DFT) was employed to assign the superatomic properties of the nanomolecule and interpret its optical properties. Bader charge analysis of the gold atoms was used to assign the geometric structure in terms of the divide-and-protect⁴⁶ concept.

EXPERIMENTAL SECTION

Materials. Thiophenol (SAFC, ≥97%) and *trans*-2-[3[(4-*tert*butylphenyl)-2-methyl-2-propenylidene]malononitrile (DCTB matrix) (Fluka, ≥99%), phenylethanethiol, NaBH_4 were purchased from Aldrich. Tetrahydrofuran (no stabilizer) and other solvents like toluene, methanol, acetonitrile, and

acetone were used from Fischer as received. Biorad BioBeads S-X1 were used for size exclusion chromatography (SEC).

Methods. UV-visible absorption spectra were recorded in toluene on a Shimadzu UV-1601 instrument in toluene. ESI-MS and MS/MS spectra were acquired on a Waters SYNAPT HDMS instrument in HPLC grade THF, without any additives present. The instrument was calibrated using $\text{Au}_{38}(\text{SC}_2\text{H}_4\text{Ph})_{24}$, which is close to the mass of $\text{Au}_{36}(\text{SPh})_{24}$. Electrochemical measurements were performed on a CHI 620 instrument using 5 mg of the title compound in 5 mL of 1,2-dichloroethane solution with 0.5 mM BTTPATBF₂₀ (bis(triphenyl phosphoranylidene) ammonium tetrakis (pentafluorophenyl)) as supporting electrolyte under a nitrogen atmosphere. The supporting electrolyte BTTPATBF₂₀ was prepared using the protocol reported before.^{47,48} Powder XRD measurements were performed on a Bruker D8-Focus XRD instrument on a quartz substrate. A 10 mg portion of sample was dissolved in a minimal amount of toluene and deposited on the substrate and air-dried.

Crystallization. A 1 mg portion of $\text{Au}_{36}(\text{SPh})_{24}$ was dissolved in 100 μL of toluene for some unrelated experiments. A 20 μL portion of this solution was used for experiments, while the rest of the solution was left unattended in an uncapped vial in the fume hood over a period of a few days. After ~2 weeks, dried crystals were observed in the bottom and side of the vial. The formation of crystals was serendipitous, but the crystals obtained were of high quality for acquiring X-ray diffraction data.

Single Crystal X-ray Analysis. A black needle crystal was selected under oil under ambient conditions and attached to the tip of a MiTeGen MicroMount. The crystal was mounted in a stream of cold nitrogen at 100 K and centered in the X-ray beam by using a video camera. The crystal evaluation and data collection were performed on a Bruker APEX II diffractometer with Mo $\text{K}\alpha$ ($\lambda = 0.71073 \text{ \AA}$) radiation. The initial cell constants were obtained from three series of ω scans at different starting angles. Each series consisted of 12 frames collected at intervals of 0.5° in a 6° range about ω with an exposure time of 20 s per frame. The reflections were successfully indexed by an automated indexing routine built in the APEXII program suite. The solution and refinement was carried out in Olex⁴⁹ using the program SHELXTL.

Crystal Data. For $\text{Au}_{36}\text{S}_{24}\text{C}_{144}\text{H}_{120}$: triclinic, space group $\overline{\text{P}1}$ (no. 2), $a = 18.554(12) \text{ \AA}$, $b = 20.370(13) \text{ \AA}$, $c = 30.482(20) \text{ \AA}$, $\alpha = 95.488(7)^\circ$, $\beta = 94.821(8)^\circ$, $\gamma = 110.991(7)^\circ$, $V = 10620(12) \text{ \AA}^3$, $z = 2$, $\mu(\text{Mo } \text{K}\alpha) = 25.02 \text{ mm}^{-1}$; $\rho_{\text{calc}} = 3.037 \text{ mg/mm}^3$, $F(000) = 8424$, $T = 100 \text{ K}$, $2\theta_{\text{max}} = 41.9^\circ$, 22386 reflections, $R(\text{int}) = 0.1178$; data/restraints/parameters = 22386/276/709; $\text{GooF} = 1.057$, $R_1 = 0.0681$, $wR_2(\text{all data}) = 0.2329$; $-2.54 < \Delta\rho < 2.19 \text{ e}/\text{\AA}^3$. CCDC number 996171.

Synthesis. A similar protocol reported by our group in the first report³⁷ on $\text{Au}_{36}(\text{SPh})_{24}$ in 2011 was used here. Briefly, the synthesis of $\text{Au}_{36}(\text{SPh})_{24}$ involves three steps. The first step is the synthesis of a crude product which is a polydisperse mixture of nanomolecules dominated by 14 and 22 kDa nanomolecules ($\text{Au}_{67}(\text{SR})_{35}$ and $\text{Au}_{103-105}(\text{SR})_{44-46}$, respectively, with R = $-\text{SCH}_2\text{CH}_2\text{Ph}$). The second step is etching the polydisperse mixture in thiophenol. The third and final step is purification of the product from the second step by size exclusion chromatography.⁵⁰

Step 1: Synthesis of Crude Product.¹⁷ For the synthesis of the crude product, 1 mmol of $\text{HAuCl}_4 \cdot 3\text{H}_2\text{O}$ was dissolved in 20 mL of tetrahydrofuran and 6 mmol of phenylethanethiol

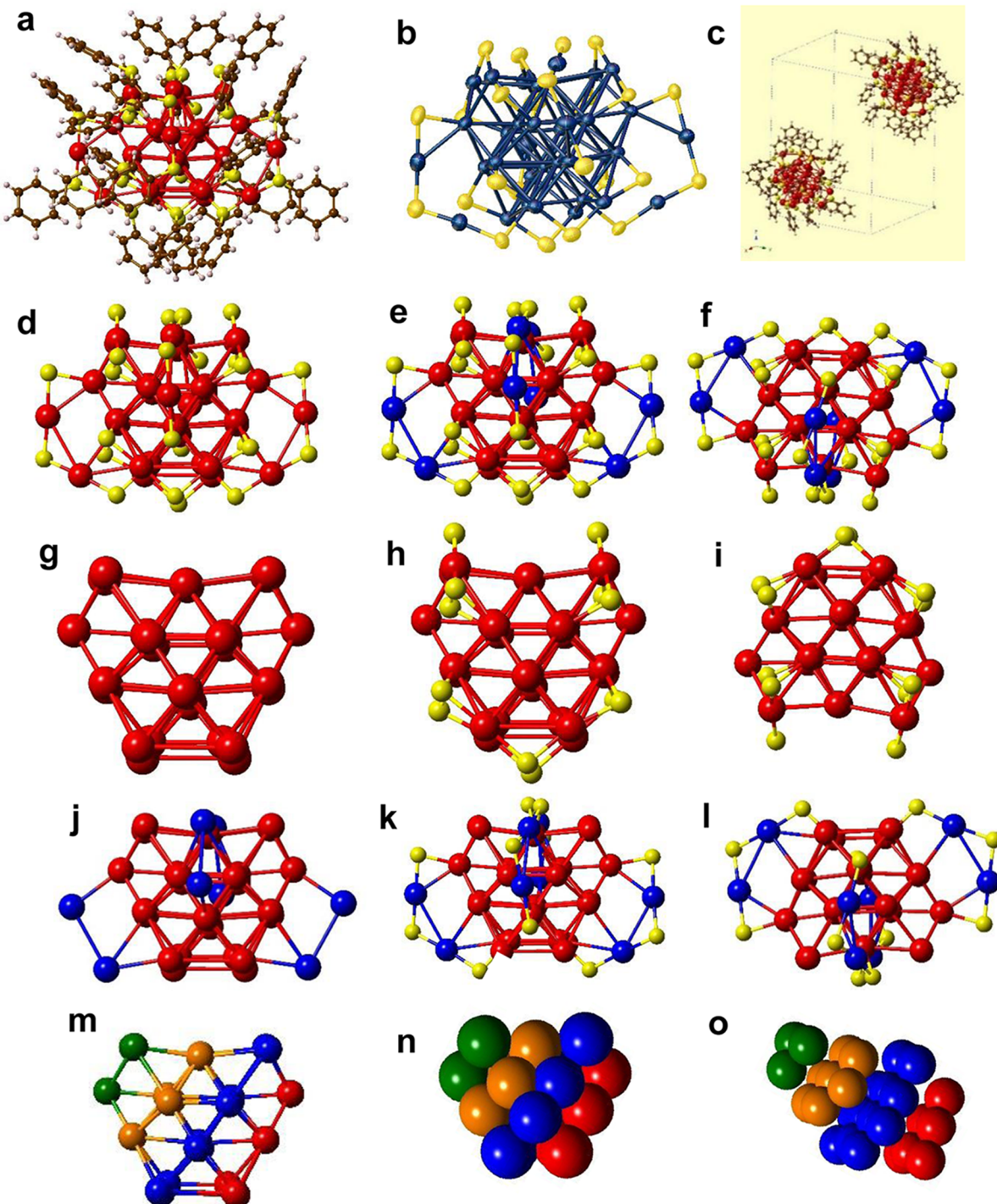


Figure 1. X-ray crystal structure of $\text{Au}_{36}(\text{SPh})_{24}$. (a) Total structure of $\text{Au}_{36}(\text{SC}_6\text{H}_5)_{24}$; (b) $\text{Au}_{36}\text{S}_{24}$ motif shown as thermal ellipsoids, illustrating the quality of the structure; (c) unit cell showing two $\text{Au}_{36}(\text{SPh})_{24}$ molecules; (d) $\text{Au}_{36}\text{S}_{24}$ motif only; (e) $\text{Au}_{36}\text{S}_{24}$ motif with the two $-\text{Au}_2\text{SR}_3-$ motifs shown in blue; (f) the structure in part e rotated by 90°; (g) Au_{28} motif only; (h) the $\text{Au}_{28}\text{S}_{12}$ motif, where the four $\text{Au}_2(\text{SR})_3$ -type motifs are observed; (i) the structure in part h rotated by 90°; (j) Au_{36} motif; (k) Au_{36} motif with the four Au_2SR_3 motifs highlighted in blue; (l) 90° rotation of the structure in part k; Au_{28} motif in ball and stick (m) and space filling model (n) displaying various layers of atoms in different colors to illustrate cubic close-packing; (o) the space filling model in part n where the various layers of atoms are artificially stretched out to display the cubic close-packing; structures in parts a and c to l are shown in ball and stick models. Coloring scheme is as follows: Au - red or blue; S - yellow; C - brown; H - pink.

($\text{HSCH}_2\text{CH}_2\text{Ph}$) was added. The reaction mixture was allowed to stir at 500 rpm for 30 min when the yellow solution became a turbid white mixture. To this solution, 10 mmol of NaBH_4 was added and the color changed from turbid to black instantly. The reaction was stirred for 5 min before the solvent was

removed via rotary evaporation. The resulting product was washed three times to remove the excess ligand and dried.¹⁷

Step 2: Etching the Crude Product in Thiophenol. The MALDI mass spectrum of the product from step 1 showed a polydisperse mixture of nanomolecules with $\text{Au}_{67}(\text{SR})_{35}$ (ref

17) and $\text{Au}_{103-105}(\text{SR})_{44-46}$ (ref 51) as dominant species.³⁷ The mixture was dissolved in 1 mL of thiophenol and heated at 80 °C for 3 h. The stirring was kept low and constant at 300 rpm. The resulting product was washed with methanol five times to remove the excess thiophenol.

Step 3: Purification of the Product. The high laser MALDI mass spectrum of the product from step 2 shows a dominant peak in the mass range 9–10 kDa for $\text{Au}_{36}(\text{SPh})_{24}$ with some minor peaks in the higher mass region. In order to remove these higher mass nanomolecules, size exclusion chromatography was performed on the above product.⁵⁰ The initial fractions had larger nanomolecules indicated by their brown color, whereas the final fractions were green indicating the purity of Au_{36} . The monodispersity of Au_{36} was also confirmed by MALDI mass spectrometry performed at high laser fluence.³⁷

Computational Details. Computations were performed using the grid-projected augmented-wave method as implemented in the GPAW package including scalar-relativistic effects for gold atoms.^{52,53} If not indicated otherwise, all calculations were done at the GGA-PBE level of theory.^{54,55} Optimizations ($\text{Au}_{36}(\text{SH})_{24}$; convergence criterion 0.05 eV/Å for each atom) and electronic structure analysis were performed using a grid spacing of $h = 0.2$ Å. Bader charge (BC) analysis was performed using the program provided by the Henkelman group.⁵⁶ Angular-momentum-resolved projected density of states (PDOS) analysis was done by projecting the Kohn–Sham (KS) wave functions into the center of mass of the nanomolecule including a radius of 3.0 Å.⁵⁷ Atom-resolved PDOS decomposition was performed by projecting the KS wave functions into each atom including a radius of 1.4 Å.⁵⁸ KS orbitals were plotted using an isosurface cutoff of 0.05.

Additional computations were run using density functional theory as implemented in the code ADF2012.01.⁵⁹ In the ADF program, the LB94 model potential⁶⁰ was used to calculate 500 excited states using linear response time-dependent density functional theory (TDDFT). A double- ζ (DZ) basis set with the frozen core approximation was used for all calculations. Relativistic effects were considered using the zeroth order regular approximation (ZORA).^{61,62} Excitation spectra were convoluted using a Lorentzian with a fwhm value of 30 nm.

RESULTS AND DISCUSSION

X-ray Crystallography. Black needles in the $P\bar{1}$ space group were solved to an R_1 value of 6.8% to yield the $\text{Au}_{36}(\text{SPh})_{24}$ composition. Figure 1a shows the total structure of $\text{Au}_{36}(\text{SPh})_{24}$. The heavy atoms, Au and S, were anisotropically refined, as shown by the thermal ellipsoids in Figure 1b. The size of the thermal ellipsoids is a good crystallographic indicator of correct atom assignment. Figure 1c shows the unit cell containing two molecules ($Z = 2$). Parts d–f of Figure 1 show the $\text{Au}_{36}\text{S}_{24}$ motif. The four $-\text{Au}_2\text{SR}_3-$ motifs are shown in blue and are rotated by 90° in Figure 1e and f. Figure 1g shows the Au_{28} core with a face-centered cubic (fcc)-like atomic arrangement. Twelve sulfur atoms bond with the Au_{28} core to form four $-\text{Au}_2\text{SR}_3-$ like motifs with this core, as seen in 0 and 90° views in Figure 1h and i. Parts j–l of Figure 1 show how the Au_{28} core is protected by the additional four $-\text{Au}_2\text{SR}_3-$ motifs shown in blue. See below for an alternative charge state analysis suggesting a Au_{20} core. The cubic close-packing of the Au_{28} motif is illustrated in both ball and stick (Figure 1m) and space filling (Figure 1n) models, where the various layers ($\text{Au}_3-\text{Au}_7-\text{Au}_{12}-\text{Au}_6 = \text{Au}_{28}$) of atoms are shown by different colors. The

layers of atoms are artificially stretched out in Figure 1o to display the cubic close-packing in the $\text{Au}_3(\text{green})-\text{Au}_7(\text{orange})-\text{Au}_{12}(\text{blue})-\text{Au}_6(\text{red})$ layers. We note that the structure and bonding of $\text{Au}_{36}(\text{SPh})_{24}$, especially the $\text{Au}_{36}\text{S}_{24}$ motif, is similar to that of the $\text{Au}_{36}\text{S}_{24}$ motifs in the previously reported^{38,39} $\text{Au}_{36}(\text{SPh}-t\text{Bu})_{24}$ and $\text{Au}_{36}(\text{SC}_5\text{H}_9)_{24}$.

Geometrically, the nanomolecule has previously been interpreted as being composed of a Au_{28} core with fcc lattice and four dimeric (SR–Au–SR–Au–SR) protecting units.^{38,40} The remaining 12 thiolates were assigned as “bridging” and not engaging in a “divide-and-protect”-type⁴⁶ of binding. Visual inspection of the nanomolecule, however, gives rise to doubt about this assignment.³⁰ Alternatively, the nanomolecule can be interpreted as being composed of a Au_{20} core that is protected with four “regular” dimeric units and an additional four “distorted” dimeric units, where the gold atoms in the “distorted” units are part of the fcc lattice. In a similar manner, the $\text{Au}_{28}(\text{SPh}-t\text{Bu})_{20}$ nanomolecule was interpreted as showing the bridged-thiolate binding motif,⁶³ while a later theoretical analysis of Au atom charges showed that these thiolates in fact belong to trimeric ((SR–Au)₃–SR) units.⁶⁴

Electronic Structure. DFT analysis of the electronic structure of $\text{Au}_{36}(\text{SR})_{24}$ shows that the nanomolecule can be understood as a 12-electron superatom complex (SAC) with a superatomic electronic configuration of $1S^2\ 1P^6\ 1D^4$ (the superatomic orbitals are formed by delocalization of the Au(6s) electrons⁵⁷). The nanomolecule consists of a tetrahedral core, and the occupation and degeneracy of the D-states is in agreement with crystal field splitting of tetrahedral complexes; i.e., $D_{x^2-y^2}$ and D_{z^2} are stabilized, while D_{xy} , D_{xz} , and D_{yz} are destabilized.

The electronic structure of $\text{Au}_{36}(\text{SPh})_{24}$ was computed at different levels of theory (PBE, LDA, and LB94). The coordinates were extracted directly from the X-ray diffraction data, and no optimization of the geometric structure was performed. For comparison, we optimized a model compound, $\text{Au}_{36}(\text{SH})_{24}$, and optimized its geometry (LDA, PBE). The HOMO–LUMO (HL) gaps of the compounds are listed in Table 1. Comparison of analogous experimental values (see

Table 1. HOMO–LUMO Gaps of $\text{Au}_{36}(\text{SPh})_{24}$ and $\text{Au}_{36}(\text{SH})_{24}$ Computed at Different Levels of Theory and Experimentally Determined Values for $\text{Au}_{36}(\text{SC}_6\text{H}_4-\text{X})_{24}$

compound	method	HL-gap (eV)
$\text{Au}_{36}(\text{SH})_{24}$	LDA	1.69
	PBE	1.82
$\text{Au}_{36}(\text{SC}_6\text{H}_4-\text{H})_{24}$	LDA	1.51
	PBE	1.57
$\text{Au}_{36}(\text{SC}_6\text{H}_4-t\text{Bu})_{24}$	LB94	1.79
	optical gap, E_g^{opt}	1.71
	DPV Echem. gap	1.96
	CV Echem. gap, E_g^{ele}	1.94
$\text{Au}_{36}(\text{SC}_6\text{H}_4-t\text{Bu})_{24}$	optical gap	1.63 ³⁸

below) with those obtained from calculations on $\text{Au}_{36}(\text{SPh})_{24}$ shows that PBE and LB94 both represent the optical gap well (1.71 eV). We did not compute the electronic structure of $\text{Au}_{36}(\text{SPh}-t\text{Bu})_{24}$ for comparison, since several atoms are lacking in the cif file of the crystal structure and optimization of the structure would give rise to additional errors.³⁸

As outlined above, visual inspection of the structure of $\text{Au}_{36}(\text{SC}_6\text{H}_4-\text{X})_{24}$ raises doubts about the assignment of 12

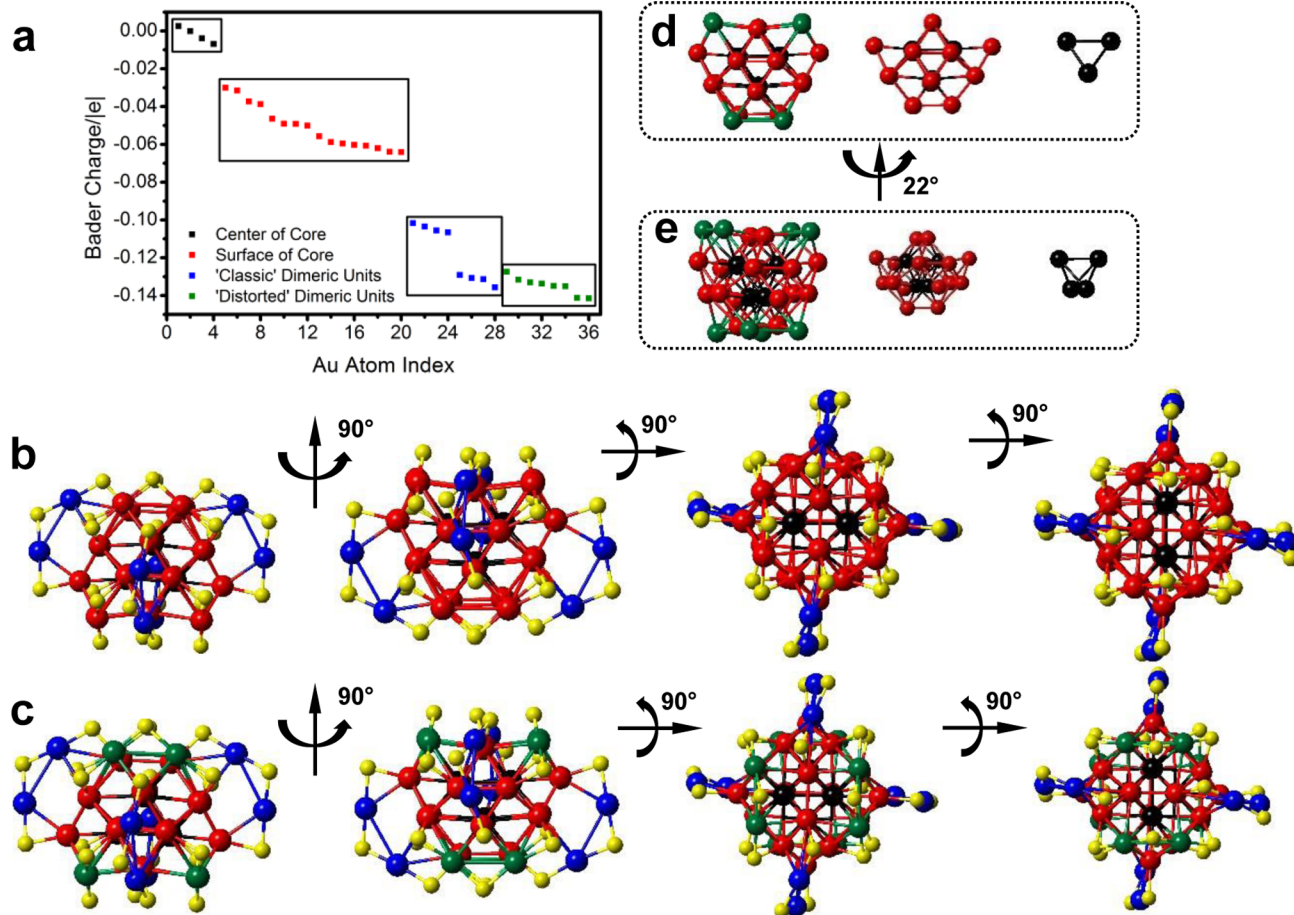


Figure 2. Bader charge analysis leads to an alternative view containing a Au_{20} core instead of a Au_{28} geometric core. (a) Bader charges of Au atoms in $\text{Au}_{36}(\text{SPh})_{24}$ computed at the PBE level of theory. The 36 Au atoms are divided into four major categories: Au_{20} (black Au₄ + red Au₁₆) + blue Au₈ + green Au₈ = 36; (b) $\text{Au}_{36}\text{S}_{24}$ motif only, where the two “classic” $-\text{Au}_2\text{SR}_3-$ motifs shown in blue are as described by the structure described from the geometric perspective in Figure 1. The three other models on the right show the structure in various orientations; (c) the $\text{Au}_{36}\text{S}_{24}$ motif, where the four $\text{Au}_2(\text{SR})_3$ -type distorted motif is shown in green; (d) left, the Au_{28} geometric motif where the 8 green Au atoms are shown to be oxidized and not part of the core based on Bader charges; (middle), the Au_{20} core motif based on Bader charges; (right) the innermost black Au₄ tetrahedral motif whose Bader charge is closest to zero; (e) the same structures shown in part d but rotated by 22° along the vertical axis for a clearer view. The coloring scheme is as follows: Au - black or red or blue or green; S - yellow.

thiolate groups binding in bridged positions to a Au_{28} core. Analogous to the analysis⁶⁴ of the structure of $\text{Au}_{28}(\text{SPh}-t\text{Bu})_{20}$,⁶³ we performed Bader charge analysis of the gold atoms in the nanomolecule. It was noted earlier that Au atoms in protecting units should be formally oxidized (+1), whereas core atoms should be neutral. Bader charge analysis should therefore reveal a clear gap between these types of Au atoms in the nanomolecule. Depending on geometric or charge state analysis based interpretation, the $\text{Au}_{36}(\text{SR})_{24}$ nanomolecule does either have a Au_{28} core (bridged binding) or a Au_{20} core (distorted dimeric units). As a benchmark for comparison, we use the Au atoms in the four “classic” dimeric units.

We identify four classes of gold atoms in the nanomolecule structure. Four atoms are in the inner core (tetrahedron), having no direct bond to sulfur atoms; see Figure 2a,d,e. An additional 16 atoms form the outer sphere of the core, binding to thiolate groups. The remaining 16 atoms can be divided into the four “classic” dimeric motifs (eight Au atoms, benchmark for oxidized Au), and the remaining eight Au atoms belong either to a putative Au_{28} core or are part of “distorted” dimeric motifs. The four core atoms have Bader charges very close to 0 (the Bader charges are normalized to the charge of the nucleus,

$z = 79$). The atoms at the surface of the nanomolecule core have slightly lower Bader charges (ca. -0.03 – -0.06 lel), indicating partial electron transfer to the electron-withdrawing thiolate groups (the lower the Bader charge, the less electron density is present at a given atom, indicating oxidation). A clear gap is identified for the eight Au atoms in the classic dimeric units (ca. -0.10 – -0.14 lel) (Figure 2a). The remaining eight gold atoms (which are the ones to be assigned either to the core or to distorted units) have Bader charges in the range of those in the classic dimeric units (ca. -0.13 – -0.14 lel), and in fact appear to be even more oxidized than the gold atoms in the classic dimeric units. These results are widely reproduced when using the LDA functional.

On the basis of the Bader charges of the gold atoms in $\text{Au}_{36}(\text{SPh})_{24}$, we assign the remaining eight gold atoms as part of distorted dimeric units, $(\text{SR}-\text{Au})_2-\text{SR}$. The gold atoms are not part of the core of the nanomolecule, reducing it from Au_{28} to Au_{20} . The nanomolecule is protected by four “classic” and four “distorted” units. Of note, a distortion is found in the “classic” units as well. The Au atoms in these are split into two groups containing four atoms each. This is caused by a slight distortion of the units in a sense that both their ends are not

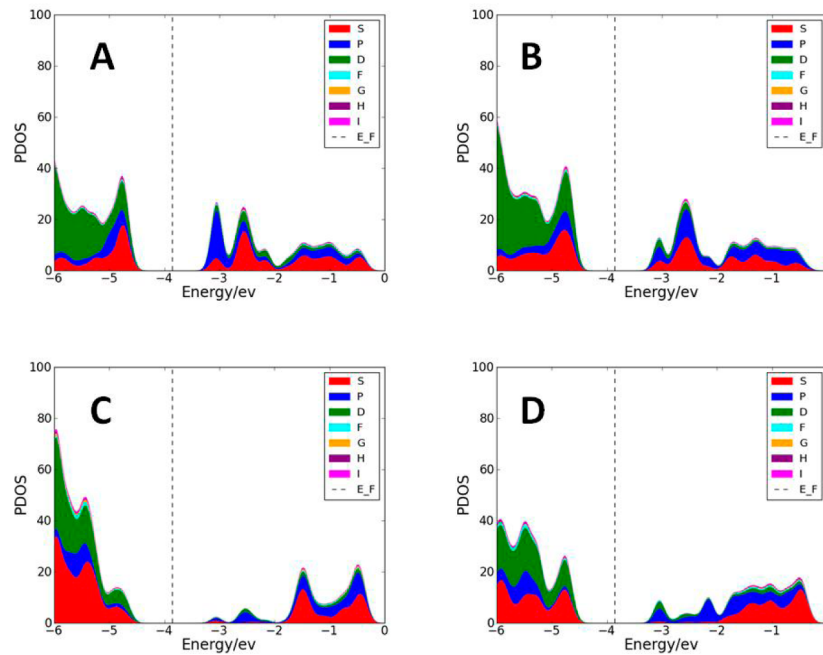


Figure 3. Angular-momentum-resolved PDOS into the Au atoms of the $\text{Au}_{36}(\text{SPh})_{24}$ nanomolecule: (A) inner core atoms; (B) core atoms at its surface; (C) Au atoms in the “classic” dimer motif; (D) Au atoms in the “distorted” dimer motif. The vertical dashed lines indicate the Fermi level of the nanomolecule.

perfectly chemically equivalent. One of the $\text{Au}_{\text{Surface}}-\text{S}$ bonds is slightly shorter than the other. This is reflected in the electronic structure of the nanomolecule, manifesting in the Bader charge of the Au adatoms neighboring the thiolate groups that bind to the surface of the core. The shortened bonds should be more polarized and make the sulfur atoms less prone to localize electron density from the neighboring adatoms. These are therefore expected to have slightly higher Bader charges (ca. -0.1 lel) than the Au adatoms next to the less polarized, longer $\text{Au}_{\text{Surface}}-\text{S}$ bonds (ca. -0.14 lel).

Furthermore, we analyze the electronic states of the individual Au atoms around the HL-gap (atom-resolved projected density of states, PDOS) with respect to their angular momentum. In general, the Au atoms in the protecting units contribute significantly less to the frontier orbitals of the nanomolecule (Figure 3). This is most pronounced for the first unoccupied states that have superatomic character (see below). This behavior is expected, since Au atoms in the units lack their 6s electron that participates in superatomic orbitals, whereas the Au atoms in the core participate in the formation of superatomic orbitals. Overall, the results are in agreement with those obtained from Bader charge analysis.

We also analyzed the nanomolecule in terms of the SAC model.⁵⁷ For convenience, we start from the Au_{20}^{8+} core of the nanomolecule. Without optimization, the electronic structure was calculated at the PBE and LB94/DZ levels of theory. The results are widely consistent. For PBE, the superatomic 1S and 1P orbitals are found well below the HOMO. Close to the HL-gap, a series of delocalized orbitals are found. Two occupied D-states are identified among the occupied states (HOMO and HOMO-4 or HOMO-1 for PBE and LB94/DZ, respectively; see Figure S1, Supporting Information). LUMO, LUMO+1, and LUMO+2 form the unoccupied D-states. LUMO+3 was identified as 2S, followed by 1F states (LUMO+4 to LUMO+10). The splitting of the D-states is consistent with a

tetrahedral crystal field splitting, and the superatomic configuration is $1\text{S}^2\ 1\text{P}^6\ 1\text{D}^4$.

Including the ligands complicates the interpretation of the electronic structure. In the model compound $\text{Au}_{36}(\text{SH})_{24}$ (PBE-optimized) and the title compound $\text{Au}_{36}(\text{SPh})_{24}$, significant mixing of Au(5d) states and the ligands into the delocalized orbitals is observed, making it less straightforward to identify the occupied D-states, while the unoccupied superatomic orbitals are clearly seen (Figure S2, Supporting Information). In $\text{Au}_{36}(\text{SPh})_{24}$, the angular-momentum-resolved PDOS clearly shows D-character around the HL-gap (Figures 3 and 4). These results are widely consistent with the interpretation of the electronic structure in an earlier report.³⁸

Optical Properties. In our earlier report on “ $\text{Au}_{36}(\text{SPh})_{23}$ ”, we have highlighted the distinct electronic features in the UV-vis region at 566 (intense peak), 370, and 430 nm (shoulder peaks). In this report, we have invoked purification procedures

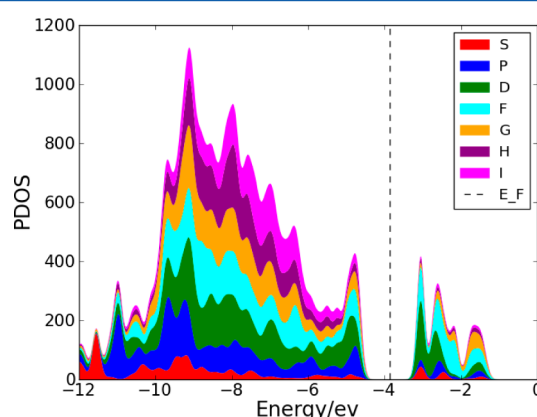


Figure 4. Angular-momentum-resolved PDOS of $\text{Au}_{36}(\text{SPh})_{24}$ (PBE level). The vertical dashed line indicates the Fermi level.

of gold nanomolecules by SEC to obtain a spectrum of higher quality (Figure 5).

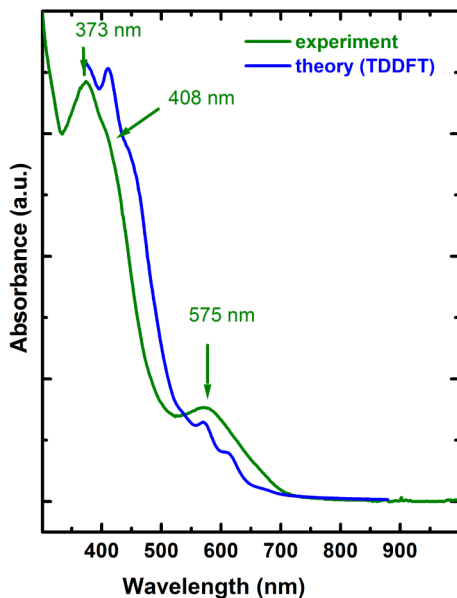


Figure 5. Experimental (green) and calculated (blue) UV-vis spectra of $\text{Au}_{36}(\text{SPh})_{24}$ showing the intense absorption peaks at 573 and 373 nm.

The optical spectrum of $\text{Au}_{36}(\text{SPh})_{24}$ has two sharp absorption bands at 575 and 373 nm. There is also a shoulder peak at 408 nm. The compound shows an absorption onset at ~ 725 nm (1.71 eV), which is in close agreement with the LB94-calculated HL-gap (1.79 eV).

The time-dependent density functional theory (TDDFT) absorption spectrum of $\text{Au}_{36}(\text{SPh})_{24}$ at the LB94/DZ level of theory is shown in Figure 5, blue spectrum. The lowest energy vertical transition occurs at 690 nm (1.79 eV), which is only 0.08 eV higher in energy than the experimental absorption onset of 720 nm (1.71 eV). This first peak arises from the HOMO \rightarrow LUMO transition (a D \rightarrow D transition), and is weak as expected for a symmetry-forbidden excitation. The first moderately strong peaks that lie in the 600–625 nm (1.98–2.07 eV) range arise primarily from a mixture of transitions out of the HOMO–2, HOMO–3, and HOMO–4 into the LUMO and LUMO+1. The strong peak at 575 nm (2.15 eV) corresponding to the experimental peak at ~ 575 nm has a dominant contribution from the HOMO–2 to LUMO+2 transition, but this excitation is also significantly influenced by transitions out of the HOMO–9 through HOMO–3 into the LUMO, LUMO+1, and LUMO+2. The 575–625 nm peaks can be classified as interband transitions, since they arise from ligand-based Au(5d) and S(3p) orbitals into the delocalized superatom D and 2S orbitals.

Three strong peaks at 475 nm ($f = 0.048$), 467 nm ($f = 0.050$), and 466 nm ($f = 0.055$) are responsible in large part for the shoulder observed around 450–475 nm in the TDDFT spectrum (which likely correlates with the experimental shoulder observed at 430 nm). These excitations primarily arise from transitions out of the HOMO–9 through HOMO–2 into the lowest set of F orbitals (LUMO+4 to LUMO+6); a small contribution to these excitations also comes from the HOMO to LUMO+7 (D \rightarrow F) transition.

Five strong excitations at 427 nm ($f = 0.073$), 415 nm ($f = 0.046$), 412 nm ($f = 0.077$), 410 nm ($f = 0.076$), and 405 nm ($f = 0.057$) are significant contributors to the strong peak that lies at 400–430 nm in the TDDFT spectrum, which may correlate to the experimental peak at 375 nm. The peaks at 415, 412, and 410 nm are dominated by the HOMO to LUMO+8 and LUMO+9 (D \rightarrow F) transitions; all peaks also have interband ligand \rightarrow superatom D or F character as well.

Contributions from transitions into the phenyl π^* orbitals are predicted to begin at wavelengths below 390 nm, which in the TDDFT spectrum lies to the blue of the bump.

Electrochemistry. The electrochemical characterization of $\text{Au}_{36}(\text{SR})_{24}$ was performed for the first time using differential pulse voltammetry (DPV), Figure 6.

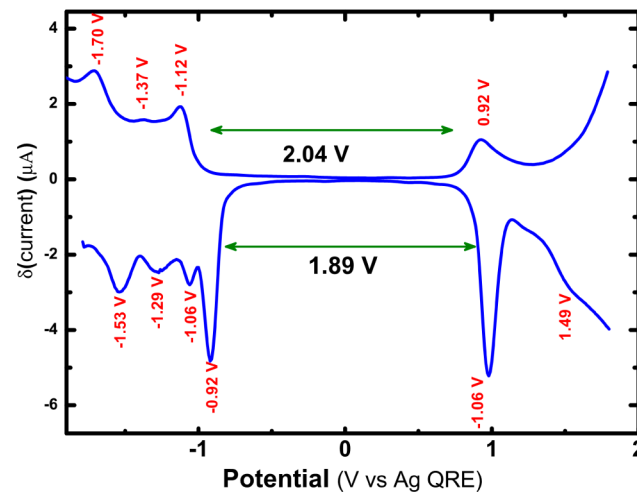


Figure 6. Differential pulse voltammetry (DPV) curve of $\text{Au}_{36}(\text{SPh})_{24}$ in dichloroethane/0.5 M BTPPATBF₂₀ as supporting electrolyte.

The electrochemical gap, which is the difference between the first oxidation and first reduction potentials, was calculated to be 1.96 eV from the DPV measurements. When corrected for the charging energy (0.23 eV),⁵ the HOMO–LUMO gap from electrochemical data is estimated to be 1.73 eV which is in close agreement with the theoretically calculated HOMO–LUMO gap. For gold nanomolecules, the electrochemical gap decreases with increasing size due to the molecule-like to bulk-metal-type transition. However, the electrochemical gap for $\text{Au}_{36}(\text{SPh})_{24}$ is so far the largest for gold nanomolecules. Note that the electrochemical gap of $\text{Au}_{36}(\text{SPh})_{24}$ is larger than that of $\text{Au}_{25}(\text{SR})_{18}$, which is 1.64 eV,⁶⁵ and that of $\text{Au}_{38}(\text{SCH}_2\text{CH}_2\text{Ph})_{24}$, which is 1.33 eV.⁶⁶ This large tunability in electrochemical potentials has great significance in the fields of catalysis⁶⁷ and dye sensitized solar cells. In the future, the electrochemical properties of the title gold nanomolecule need to be compared with other aromatic thiolate-protected gold nanomolecules and other Au_{36} core sized molecules.

$\text{Au}_{36}(\text{SPh})_{24}$ was further electrochemically characterized through cyclic voltammetry (CV) with ferrocene as an internal reference (Figure 7). The first oxidation and first reduction potentials were found to be semireversible in dichloromethane with a sweep rate of 100 mV/s. The first oxidation potential was taken to be 0.55 V vs ferrocene/ferrocenium (Fc/Fc^+). The first reduction potential was taken as -1.39 V vs Fc/Fc^+ to give an electrochemical bandgap of 1.94 eV.

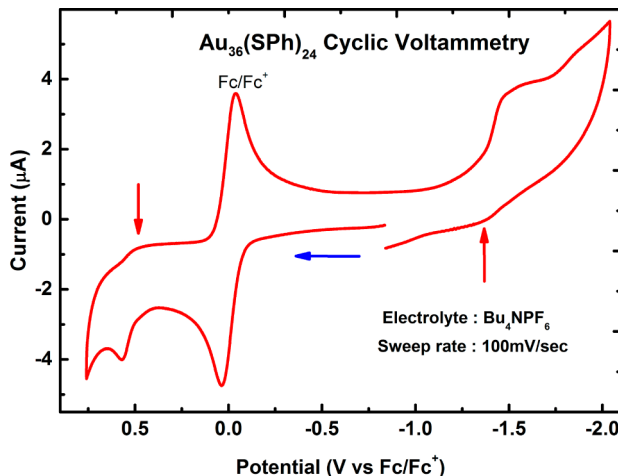


Figure 7. Cyclic voltammetry sweep of $\text{Au}_{36}(\text{SPh})_{24}$ in dichloromethane with Bu_4NPF_6 (0.1 M) as electrolyte with a scan rate of 100 mV/s. Ferrocene was used as an internal standard with the sweep direction set first toward positive potentials (blue arrow). The red arrows represent the semireversible oxidation and reduction potentials of $\text{Au}_{36}(\text{SPh})_{24}$.

The comparison of the computational HOMO–LUMO gap can only be performed through experimental approximations, whereas the LUMO is a virtual orbital (i.e., a nonobservable).⁶⁸ The LUMO energy level must first be perturbed in order to be observed, whereas it is a nonoccupied theoretical entity (Figure 8). Common solution-based experimental approximations are

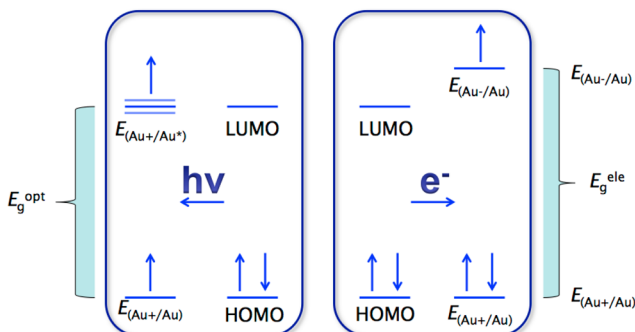


Figure 8. Energy level depiction for the photoexcitation (left) and the electrochemical reduction (right) of a ground-state molecule.

either (1) through the electrochemical oxidation potential ($E_{(\text{Au}+/ \text{Au})}$) and the optical energy gap (E_g^{opt}) through the equation $E_{(\text{M}+/ \text{M}^*)} = E_{(\text{M}+/ \text{M})} - E_g^{\text{opt}}$, where M = molecule and $E_{(\text{M}+/ \text{M}^*)}$ is the excited-state oxidation potential (a LUMO related, measurable value), or (2) through the electrochemical reduction potential ($E_{(\text{M}-/ \text{M})}$), which is a separate measurable LUMO related value. It is important to note that these two values often differ for a given compound, whereas the potentials of these energy levels are not strictly related (Figure 8). Commonly, the $E_{(\text{M}-/ \text{M})}$ energy level is higher in energy due largely to electron repulsion (i.e., a larger electrochemical gap); however, there are examples where the molecules strongly stabilize electron density and the $E_{(\text{M}-/ \text{M})}$ is lower in energy than the $E_{(\text{M}+/ \text{M})}$.⁶⁹ Importantly, computational and experimental data can only be reported as an approximation to these experimental values and thus the differences pointed out above are to be expected.

Revision to the $\text{Au}_{36}(\text{SPh})_{24}$ Formula. In the case of $\text{Au}_{36}(\text{SC}_6\text{H}_4-t\text{Bu})_{24}$, the synthesis involved ligand exchange on a pure sample of $\text{Au}_{38}(\text{SCH}_2\text{CH}_2\text{Ph})_{24}$ ⁷⁰ in contrast to the polydisperse mixture of Au_{67} and Au_{104} mixture used by our group in making “ $\text{Au}_{36}(\text{SPh})_{23}$ ”. The assignment of $\text{Au}_{36}(\text{SC}_6\text{H}_4-t\text{Bu})_{24}$ was confirmed by high resolution ESI-MS and the crystal structure. The assignment of “ $\text{Au}_{36}(\text{SPh})_{23}$ ” was from a relatively low resolution MALDI-MS analysis.^{5,7,72} HS-C₆H₄-tBu is a derivative of thiophenol and is believed to have similar chemical reactivity on gold nanomolecules unless the bulkiness of the *tert*-butyl group affects it otherwise. Due to the similar aromatic ligands involved and common absorption features at ~ 570 , ~ 430 , and ~ 370 nm of the nanomolecules in both the reports, both “ $\text{Au}_{36}(\text{SPh})_{23}$ ” and $\text{Au}_{36}(\text{SC}_6\text{H}_4-t\text{Bu})_{24}$ have the same core geometry and composition and “ $\text{Au}_{36}(\text{SPh})_{23}$ ” has always been $\text{Au}_{36}(\text{SPh})_{24}$. Figure 9 below

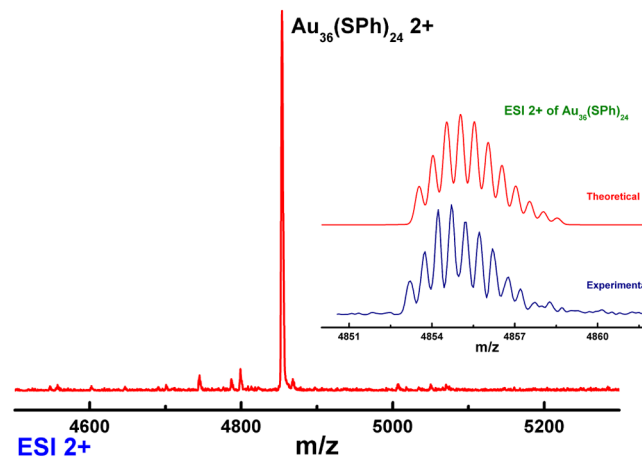


Figure 9. ESI-MS of the 2+ peak of $\text{Au}_{36}(\text{SPh})_{24}$ at m/z 4854. The inset shows the isotopic pattern match for the theoretically obtained and experimentally derived mass of $\text{Au}_{36}(\text{SPh})_{24}^{2+}$.

shows the 2+ peak of $\text{Au}_{36}(\text{SPh})_{24}$ at m/z 4855 observed in ESI-MS analysis. No peak was observed for $\text{Au}_{36}(\text{SPh})_{23}$ at m/z 4800. The experimentally observed peak for $\text{Au}_{36}(\text{SPh})_{24}$ shows a good match with the theoretical isotopic pattern (shown in the inset, Figure 9), adding further confidence to the $\text{Au}_{36}(\text{SPh})_{24}$ assignment.

Fragmentation of $\text{Au}_{36}(\text{SPh})_{24}$ in MALDI versus ESI. If the correct molecular assignment for this nanomolecule is (36, 24), then a question arises as to why the (36, 23) peak at m/z 9601 is reproducibly observed in the MALDI. A possible explanation might be that it is arising from the fragmentation of (36, 24). To study this, we have intentionally induced fragmentation, as demonstrated before,⁷³ of (36, 24) in ESI-MS. This is performed by MS/MS, where it is possible to select a single peak in the mass spectrometer and fragment it. After selecting the peak at m/z 4855 for MS/MS, the trap collision energy was systematically increased to induce fragmentation while the other parameters were maintained the same (shown in the Supporting Information). The fragmentation pattern observed is shown in Figure 10.

There are two interesting aspects of this fragmentation pattern. First, the Au_{4L_4} loss is the same as seen previously in the cases of Au_{25} and Au_{38} with MALDI-MS. Second, no fragment loss of one ligand was observed to give a $\text{Au}_{36}(\text{SPh})_{23}$ peak at m/z 4800 with ESI-MS. This indicates that fragmentation to form (36, 23) appears to be specific to

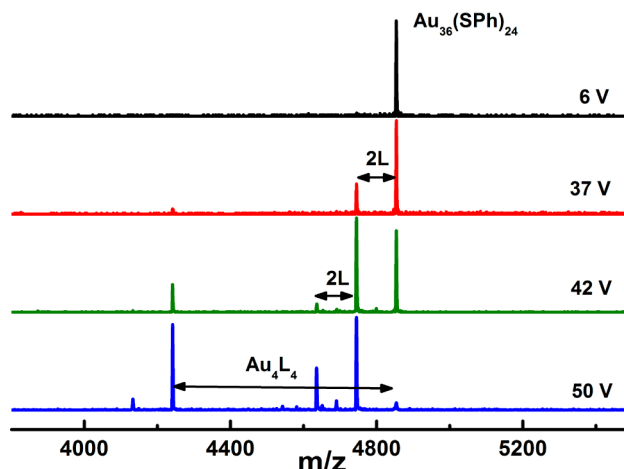


Figure 10. Positive mode ESI Q-TOF MS/MS analysis on the 2+ peak of $\text{Au}_{36}(\text{SPh})_{24}$ at m/z 4854 showing the systematic fragment loss of 2L ($L = \text{PhS}^-$, MW = 110 Da), 4L, and Au_4L_4 with increasing trap collision energy (shown to the right of each spectrum).

MALDI-MS, as noted before. The first report of Jin's group³⁸ on $\text{Au}_{36}(\text{SC}_6\text{H}_4-t\text{Bu})_{24}$ did not include any MALDI data, which would have clearly pointed out that $\text{Au}_{36}(\text{SC}_6\text{H}_4-t\text{Bu})_{24}$ is the same compound as the previously reported " $\text{Au}_{36}(\text{SPh})_{24}$ ". A subsequent work reported³⁹ by their group showed the same fragmentation pattern, with a loss of one ligand to form $\text{Au}_{36}(\text{SC}_6\text{H}_4-t\text{Bu})_{23}$, in the MALDI-MS analysis of $\text{Au}_{36}(\text{SC}_6\text{H}_4-t\text{Bu})_{24}$. To the best of our knowledge, this fragmentation pattern was never observed for any other nanomolecule before. On the basis of the X-ray crystallography and electrospray MS results, we conclude that the composition is $\text{Au}_{36}(\text{SPh})_{24}$.

Powder-XRD. Synthesis of monodisperse $\text{Au}_{36}(\text{SPh})_{24}$ in high yields has allowed for characterization studies like powder-XRD. The diffraction pattern obtained for $\text{Au}_{36}(\text{SPh})_{24}$ is compared to the theoretical pattern for an fcc core in Figure 11.

The blue spectrum represents the powder-XRD pattern for Au_{67} , while the one in red is for $\text{Au}_{36}(\text{SPh})_{24}$. X-ray crystallographic data is based on experimentation on one

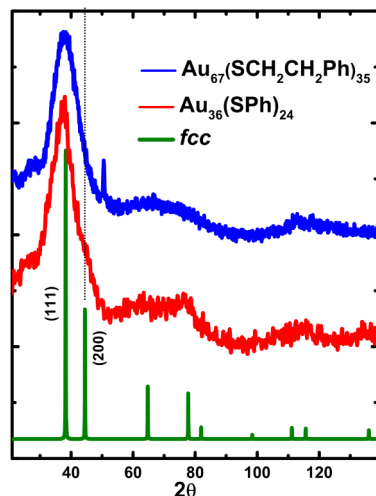


Figure 11. Powder X-ray diffraction pattern for $\text{Au}_{36}(\text{SPh})_{24}$ (red) in comparison with $\text{Au}_{67}(\text{SR})_{35}$ (blue) and fcc (green lines). $\text{Au}_{36}(\text{SPh})_{24}$ shows a minor feature at 44° corresponding to the (200) plane.

crystal, whereas the powder-XRD data takes into account many particulates in powder form. The region of the Au_{36} pattern at $2\theta = 44^\circ$ is interesting in that there is a shoulder adjacent to the main peak at 38° . This is a feature typical for fcc core geometry. This pattern points to an fcc core for Au_{36} and is in agreement with the conclusions obtained from the single crystal XRD. This geometry is quite different from the $\text{Au}_{38}(\text{SCH}_2\text{CH}_2\text{Ph})_{24}$ nanomolecule, though the difference between the composition of these two is only two Au atoms. The powder X-ray diffraction results not only agree with the single crystal X-ray diffraction data but also demonstrate the reliability of the powder diffraction technique where single crystals of gold nanomolecules are not achievable.

SUMMARY

In this work, we present an X-ray crystal structure of the phenylthiolate-stabilized $\text{Au}_{36}(\text{SPh})_{24}$ nanomolecule, and the geometric features of this system are found to be insensitive to the ligand. Powder-XRD characterization of this system is also in agreement with a fcc core. Analysis based on Bader charges suggests that the geometric structure of this system is best considered as an Au_{20} core protected by four classic dimeric units and four "distorted" dimeric units whose gold atoms enlarge the fcc core. The electronic structure of the system displays D superatomic orbitals (albeit hybridized with ligand-based orbitals) that are split by the approximate tetrahedral symmetry of the system. TDDFT calculations of the optical absorption closely match the experimental spectrum and permit assignment of the transitions. The electrochemical and optical band-gaps are uniquely wide for $\text{Au}_{36}(\text{SPh})_{24}$ when compared with other larger and smaller Au-core sizes. These unique properties will likely fuel future applications in solar energy and catalysis. Additionally, we have demonstrated that $\text{Au}_{36}(\text{SPh})_{24}$ uniquely fragments under MALDI-MS analysis to give $\text{Au}_{36}(\text{SPh})_{23}$, while under ESI-MS analysis no single-ligand dissociated masses are observed.

ASSOCIATED CONTENT

Supporting Information

Kohn–Sham orbitals and orbitals energies, the crystal structure data, and the cif file. CCDC number is 996171. This material is available free of charge via the Internet at <http://pubs.acs.org>.

AUTHOR INFORMATION

Corresponding Author

*E-mail: amal@olemiss.edu.

Notes

The authors declare no competing financial interest.

ACKNOWLEDGMENTS

The experimental work was funded by NSF-CHE-1255519. We thank Dr. Ilia Guzei for assistance with single crystal XRD analysis. C.M.A. thanks the National Science Foundation for funding under Grant No. CHE-1213771. S.K. is grateful to the German Academic Exchange Service (DAAD) for financial support and CSC – IT Center for Science (Espoo, Finland) for computational resources. Computations were performed on the FGI-grid node *Electra* at University of Jyväskylä and CSC and at Kansas State University. Prof. Hannu Häkkinen is acknowledged for discussions regarding the theoretical analysis. We thank the reviewers for the suggestion to include the timeline on the history of $\text{Au}_{36}(\text{SPh})_{24}$.

■ REFERENCES

- (1) Maity, P.; Xie, S.; Yamauchi, M.; Tsukuda, T. Stabilized Gold Clusters: From Isolation Toward Controlled Synthesis. *Nanoscale* **2012**, *4*, 4027–4037.
- (2) Hakkinen, H. The Gold-sulfur Interface at the Nanoscale. *Nat. Chem.* **2012**, *4*, 443–455.
- (3) Whetten, R. L.; Khouri, J. T.; Alvarez, M. M.; Murthy, S.; Vezmar, I.; Wang, Z. L.; Stephens, P. W.; Cleveland, C. L.; Luedtke, W. D.; Landman, U. Nanocrystal Gold Molecules. *Adv. Mater.* **1996**, *8*, 428–433.
- (4) Alvarez, M. M.; Khouri, J. T.; Schaaff, T. G.; Shafiqullin, M. N.; Vezmar, I.; Whetten, R. L. Optical Absorption Spectra of Nanocrystal Gold Molecules. *J. Phys. Chem. B* **1997**, *101*, 3706–3712.
- (5) Heaven, M. W.; Dass, A.; White, P. S.; Holt, K. M.; Murray, R. W. Crystal Structure of the Gold Nanoparticle $[N(C_8H_{17})_4]^-[Au_{25}(SCH_2CH_2Ph)_{18}]$. *J. Am. Chem. Soc.* **2008**, *130*, 3754–3755.
- (6) Chen, W.; Chen, S. Oxygen Electroreduction Catalyzed by Gold Nanoclusters: Strong Core Size Effects. *Angew. Chem., Int. Ed.* **2009**, *48*, 4386–4389.
- (7) Sousa, A. A.; Morgan, J. T.; Brown, P. H.; Adams, A.; Jayasekara, M. P. S.; Zhang, G.; Ackerson, C. J.; Kruhlak, M. J.; Leapman, R. D. Synthesis, Characterization, and Direct Intracellular Imaging of Ultrasmall and Uniform Glutathione-Coated Gold Nanoparticles. *Small* **2012**, *8*, 2277–2286.
- (8) Ackerson, C. J.; Sykes, M. T.; Kornberg, R. D. Defined DNA/nanoparticle Conjugates. *Proc. Natl. Acad. Sci. U. S. A.* **2005**, *102*, 13383–13385.
- (9) Bowman, M.-C.; Ballard, T. E.; Ackerson, C. J.; Feldheim, D. L.; Margolis, D. M.; Melander, C. Inhibition of HIV Fusion with Multivalent Gold Nanoparticles. *J. Am. Chem. Soc.* **2008**, *130*, 6896–6897.
- (10) Schaaff, T. G.; Shafiqullin, M. N.; Khouri, J. T.; Vezmar, I.; Whetten, R. L.; Cullen, W. G.; First, P. N.; Gutierrez-Wing, C.; Ascensio, J.; Jose-Yacaman, M. J. Isolation of Smaller Nanocrystal Au Molecules: Robust Quantum Effects in Optical Spectra. *J. Phys. Chem. B* **1997**, *101*, 7885–7891.
- (11) Qian, H.; Zhu, M.; Wu, Z.; Jin, R. Quantum Sized Gold Nanoclusters with Atomic Precision. *Acc. Chem. Res.* **2012**, *45*, 1470–1479.
- (12) Jazdinsky, P. D.; Calero, G.; Ackerson, C. J.; Bushnell, D. A.; Kornberg, R. D. Structure of a Thiol Monolayer-protected Gold Nanoparticle at 1.1 Ångstrom Resolution. *Science* **2007**, *318*, 430–433.
- (13) Heaven, M. W.; Dass, A.; White, P. S.; Holt, K. M.; Murray, R. W. Crystal Structure of the Gold Nanoparticle $[N(C_8H_{17})_4]^-[Au_{25}(SCH_2CH_2Ph)_{18}]$. *J. Am. Chem. Soc.* **2008**, *130*, 3754–3755.
- (14) Parker, J. F.; Fields-Zinna, C. A.; Murray, R. W. The Story of a Monodisperse Gold Nanoparticle: $Au_{25}L_{18}$. *Acc. Chem. Res.* **2010**, *43*, 1289–1296.
- (15) Chaki, N. K.; Negishi, Y.; Tsunoyama, H.; Shichibu, Y.; Tsukuda, T. Ubiquitous 8 and 29 kDa gold: Alkanethiolate Cluster Compounds: Mass-spectrometric Determination of Molecular Formulas and Structural Implications. *J. Am. Chem. Soc.* **2008**, *130*, 8608–8610.
- (16) Negishi, Y.; Chaki, N. K.; Shichibu, Y.; Whetten, R. L.; Tsukuda, T. Origin of Magic Stability of Thiolated Gold Clusters: A Case Study on $Au_{25}(SC_6H_{13})_{18}$. *J. Am. Chem. Soc.* **2007**, *129*, 11322–11323.
- (17) Nimmala, P. R.; Yoon, B.; Whetten, R. L.; Landman, U.; Dass, A. $Au_{67}(SR)_{35}$ Nanomolecules: Characteristic Size-Specific Optical, Electrochemical, Structural Properties and First-Principles Theoretical Analysis. *J. Phys. Chem. A* **2013**, *117*, 504–517.
- (18) Fields-Zinna, C. A.; Sardar, R.; Beasley, C. A.; Murray, R. W. Electrospray Ionization Mass Spectrometry of Intrinsically Cationized Nanoparticles, $[Au_{144/146}(SC_{11}H_{22}N(CH_2CH_3)_3^+)_x(S(CH_2)_5CH_3)_y]^{x+}$. *J. Am. Chem. Soc.* **2009**, *131*, 16266–16271.
- (19) Qian, H.; Jin, R. Controlling Nanoparticles with Atomic Precision: The Case of $Au_{144}(SCH_2CH_2Ph)_{60}$. *Nano Lett.* **2009**, *9*, 4083–4087.
- (20) Chen, S. W.; Murray, R. W. Arenethiolate Monolayer-protected Gold Clusters. *Langmuir* **1999**, *15*, 682–689.
- (21) Kumara, C.; Dass, A. $Au_{329}(SR)_{84}$ Nanomolecules: Compositional Assignment of the 76.3 kDa Plasmonic Faradaurates. *Anal. Chem.* **2014**, *86*, 4227–4232.
- (22) Kumara, C.; Zuo, X.; Ilavsky, J.; Chapman, K. W.; Cullen, D. A.; Dass, A. Super-Stable, Highly Monodisperse Plasmonic Faradaurate-500 Nanocrystals with 500 Gold Atoms: $Au_{\sim 500}(SR)_{\sim 120}$. *J. Am. Chem. Soc.* **2014**, *136*, 7410–7417.
- (23) Kumara, C.; Zuo, X.; Cullen, D. A.; Dass, A. Faradaurate-940: Synthesis, Mass Spectrometry, Electron Microscopy, High-Energy X-ray Diffraction, and X-ray Scattering Study of $Au_{\sim 940 \pm 20}(SR)_{\sim 160 \pm 4}$ Nanocrystals. *ACS Nano* **2014**, *8*, 6431–6439.
- (24) Dainese, T.; Antonello, S.; Gascón, J. A.; Pan, F.; Perera, N. V.; Ruzzi, M.; Venzo, A.; Zoleo, A.; Rissanen, K.; Maran, F. $Au_{25}(SEt)_{18}$, a Nearly Naked Thiolate-Protected Au_{25} Cluster: Structural Analysis by Single Crystal X-ray Crystallography and Electron Nuclear Double Resonance. *ACS Nano* **2014**, *8*, 3904–3912.
- (25) Yu, Y.; Luo, Z.; Yu, Y.; Lee, J. Y.; Xie, J. Observation of Cluster Size Growth in CO-Directed Synthesis of $Au_{25}(SR)_{18}$ Nanoclusters. *ACS Nano* **2012**, *6*, 7920–7927.
- (26) Udayabaskarao, T.; Pradeep, T. New Protocols for the Synthesis of Stable Ag and Au Nanocluster Molecules. *J. Phys. Chem. Lett.* **2013**, *4*, 1553–1564.
- (27) Pei, Y.; Zeng, X. C. Investigating the Structural Evolution of Thiolate Protected Gold Clusters from First-principles. *Nanoscale* **2012**, *4*, 4054–4072.
- (28) Heinecke, C. L.; Ni, T. W.; Malola, S.; Mäkinen, V.; Wong, O. A.; Häkkinen, H.; Ackerson, C. J. Structural and Theoretical Basis for Ligand Exchange on Thiolate Monolayer Protected Gold Nanoclusters. *J. Am. Chem. Soc.* **2012**, *134*, 13316–13322.
- (29) Aikens, C. M. Electronic Structure of Ligand-Passivated Gold and Silver Nanoclusters. *J. Phys. Chem. Lett.* **2010**, *2*, 99–104.
- (30) Jiang, D.-e. The Expanding Universe of Thiolated Gold Nanoclusters and Beyond. *Nanoscale* **2013**, *5*, 7149–7160.
- (31) Jin, R. Quantum Sized, Thiolate-protected Gold Nanoclusters. *Nanoscale* **2010**, *2*, 343–362.
- (32) Kurashige, W.; Yamaguchi, M.; Nobusada, K.; Negishi, Y. Ligand-Induced Stability of Gold Nanoclusters: Thiolate versus Selenolate. *J. Phys. Chem. Lett.* **2012**, *3*, 2649–2652.
- (33) Shibu, E. S.; Muhammed, M. A. H.; Tsukuda, T.; Pradeep, T. Ligand Exchange of $Au_{25}SG_{18}$ Leading to Functionalized Gold Clusters: Spectroscopy, Kinetics, and Luminescence. *J. Phys. Chem. C* **2008**, *112*, 12168–12176.
- (34) Whetten, R. L.; Price, R. C. Nano-golden Order. *Science* **2007**, *318*, 407–408.
- (35) Song, Y.; Wang, S.; Zhang, J.; Kang, X.; Chen, S.; Li, P.; Sheng, H.; Zhu, M. Crystal Structure of Selenolate-Protected $Au_{24}(SeR)_{20}$ Nanocluster. *J. Am. Chem. Soc.* **2014**, *136*, 2963–2965.
- (36) Price, R. C.; Whetten, R. L. All-aromatic, Nanometer-scale, Gold-cluster Thiolate Complexes. *J. Am. Chem. Soc.* **2005**, *127*, 13750–13751.
- (37) Nimmala, P. R.; Dass, A. $Au_{36}(SPh)_{23}$ Nanomolecules. *J. Am. Chem. Soc.* **2011**, *133*, 9175–9177.
- (38) Zeng, C.; Qian, H.; Li, T.; Li, G.; Rosi, N. L.; Yoon, B.; Barnett, R. N.; Whetten, R. L.; Landman, U.; Jin, R. Total Structure and Electronic Properties of the Gold Nanocrystal $Au_{36}(SR)_{24}$. *Angew. Chem., Int. Ed.* **2012**, *51*, 13114–13118.
- (39) Zeng, C.; Liu, C.; Pei, Y.; Jin, R. Thiol Ligand-Induced Transformation of $Au_{38}(SC_2H_4Ph)_{24}$ to $Au_{36}(SPh-t-Bu)_{24}$. *ACS Nano* **2013**, *7*, 6138–6145.
- (40) Das, A.; Liu, C.; Zeng, C.; Li, G.; Li, T.; Rosi, N. L.; Jin, R. Cyclopentanethiolato-Protected $Au_{36}(SC_5H_9)_{24}$ Nanocluster: Crystal Structure and Implications for the Steric and Electronic Effects of Ligand. *J. Phys. Chem. A* **2014**, *118*, 8264–8269.
- (41) Nishigaki, J.-i.; Tsunoyama, R.; Tsunoyama, H.; Ichikuni, N.; Yamazoe, S.; Negishi, Y.; Ito, M.; Matsuo, T.; Tamao, K.; Tsukuda, T. A New Binding Motif of Sterically Demanding Thiolates on a Gold Cluster. *J. Am. Chem. Soc.* **2012**, *134*, 14295–14297.
- (42) Crasto, D.; Dass, A. Green Gold: $Au_{30}(S-t-C_4H_9)_{18}$ Molecules. *J. Phys. Chem. C* **2013**, *117*, 22094–22097.

- (43) Krommenhoek, P. J.; Wang, J.; Hentz, N.; Johnston-Peck, A. C.; Kozek, K. A.; Kalyuzhny, G.; Tracy, J. B. Bulky Adamantanethiolate and Cyclohexanethiolate Ligands Favor Smaller Gold Nanoparticles with Altered Discrete Sizes. *ACS Nano* **2012**, *6*, 4903–4911.
- (44) Yang, H.; Wang, Y.; Huang, H.; Gell, L.; Lehtovaara, L.; Malola, S.; Häkkinen, H.; Zheng, N. All-thiol-stabilized Ag_{44} and $\text{Au}_{12}\text{Ag}_{32}$ Nanoparticles with Single-crystal Structures. *Nat. Commun.* **2013**, *4*, No. 2422.
- (45) Desiréddy, A.; Conn, B. E.; Guo, J.; Yoon, B.; Barnett, R. N.; Monahan, B. M.; Kirschbaum, K.; Griffith, W. P.; Whetten, R. L.; Landman, U.; Bigioni, T. P. Ultrastable silver nanoparticles. *Nature* **2013**, *501*, 399–402.
- (46) Häkkinen, H.; Walter, M.; Gronbeck, H. Divide and protect: Capping Gold Nanoclusters with Molecular Gold-thiolate Rings. *J. Phys. Chem. B* **2006**, *110*, 9927–9931.
- (47) Quinn, B. M.; Liljeroth, P.; Ruiz, V.; Laaksonen, T.; Kontturi, K. S. Electrochemical Resolution of 15 Oxidation States for Monolayer Protected Gold Nanoparticles. *J. Am. Chem. Soc.* **2003**, *125*, 6644–6645.
- (48) J. Fermin, D.; Dung Duong, H.; Ding, Z.; Brevet, o.; H. Girault, H. Photoinduced Electron Transfer at Liquid/liquid Interfaces Part II. A Study of the Electron Transfer and Recombination Dynamics by Intensity Modulated Photocurrent Spectroscopy (IMPS). *Phys. Chem. Chem. Phys.* **1999**, *1*, 1461–1467.
- (49) Dolomanov, O. V.; Bourhis, L. J.; Gildea, R. J.; Howard, J. A. K.; Puschmann, H. OLEX2: A Complete Structure Solution, Refinement and Analysis Program. *J. Appl. Crystallogr.* **2009**, *42*, 339–341.
- (50) Knoppe, S.; Boudon, J.; Dolamic, I.; Dass, A.; Bürgi, T. Size Exclusion Chromatography for Semipreparative Scale Separation of $\text{Au}_{38}(\text{SR})_{24}$ and $\text{Au}_{40}(\text{SR})_{24}$ and Larger Clusters. *Anal. Chem.* **2011**, *83*, 5056–5061.
- (51) Dass, A.; Nimmala, P. R.; Jupally, V. R.; Kothalawala, N. $\text{Au}_{103}(\text{SR})_{45}$, $\text{Au}_{104}(\text{SR})_{45}$, $\text{Au}_{104}(\text{SR})_{46}$ and $\text{Au}_{105}(\text{SR})_{46}$ Nanoclusters. *Nanoscale* **2013**, *5*, 12082–12085.
- (52) Mortensen, J.; Hansen, L.; Jacobsen, K. Real-space Grid Implementation of the Projector Augmented Wave Method. *Phys. Rev. B* **2005**, *71*.
- (53) Enkovaara, J.; Rostgaard, C.; Mortensen, J. J.; Chen, J.; Dulak, M.; Ferrighi, L.; Gavnhold, J.; Glinsvad, C.; Haikola, V.; Hansen, H. A.; et al. Electronic Structure Calculations with GPAW: a Real-space Implementation of the Projector Augmented-wave Method. *J. Phys.: Condens. Matter* **2010**, *22*, 253202.
- (54) Perdew, J. P.; Burke, K.; Ernzerhof, M. Generalized Gradient Approximation Made Simple. *Phys. Rev. Lett.* **1996**, *77*, 3865–3868.
- (55) Perdew, J. P.; Burke, K.; Ernzerhof, M. Generalized Gradient Approximation Made Simple. *Phys. Rev. Lett.* **1997**, *78*, 1396–1396.
- (56) Tang, W.; Sanville, E.; Henkelman, G. A Grid-based Bader Analysis Algorithm Without Lattice Bias. *J. Phys.: Condens. Matter* **2009**, *21*, 084204.
- (57) Walter, M.; Akola, J.; Lopez-Acevedo, O.; Jaszinsky, P. D.; Calero, G.; Ackerson, C. J.; Whetten, R. L.; Gronbeck, H.; Häkkinen, H. A Unified View of Ligand-protected Gold Clusters as Superatom Complexes. *Proc. Natl. Acad. Sci. U. S. A.* **2008**, *105*, 9157–62.
- (58) Lopez-Acevedo, O.; Tsunoyama, H.; Tsukuda, T.; Häkkinen, H.; Aikens, C. M. Chirality and Electronic Structure of the Thiolate-Protected Au_{38} Nanocluster. *J. Am. Chem. Soc.* **2010**, *132*, 8210–8.
- (59) te Velde, G.; Bickelhaupt, F. M.; Baerends, E. J.; Fonseca Guerra, C.; van Gisbergen, S. J. A.; Snijders, J. G.; Ziegler, T. Chemistry with ADF. *J. Comput. Chem.* **2001**, *22*, 931–967.
- (60) van Leeuwen, R.; Baerends, E. J. Exchange-Correlation Potential with Correct Asymptotic Behavior. *Phys. Rev. A* **1994**, *49*, 2421–2431.
- (61) van Lenthe, E.; Baerends, E. J.; Snijders, J. G. Relativistic Total Energy using Regular Approximations. *J. Chem. Phys.* **1994**, *101*, 9783–9792.
- (62) van Lenthe, E.; Ehlers, A.; Baerends, E.-J. Geometry Optimizations in the Zero Order Regular Approximation for Relativistic Effects. *J. Chem. Phys.* **1999**, *110*, 8943–8953.
- (63) Zeng, C.; Li, T.; Das, A.; Rosi, N. L.; Jin, R. Chiral Structure of Thiolate-Protected 28-Gold-Atom Nanocluster Determined by X-ray Crystallography. *J. Am. Chem. Soc.* **2013**, *135*, 10011–10013.
- (64) Knoppe, S.; Malola, S.; Lehtovaara, L.; Burgi, T.; Häkkinen, H. Electronic structure and optical properties of the thiolate-protected $\text{Au}_{28}(\text{SMe})_{20}$ cluster. *J. Phys. Chem. A* **2013**, *117*, 10526–33.
- (65) Antonello, S.; Holm, A. H.; Instuli, E.; Maran, F. Molecular Electron-Transfer Properties of Au_{38} Clusters. *J. Am. Chem. Soc.* **2007**, *129*, 9836–9837.
- (66) Toikkanen, O.; Carlsson, S.; Dass, A.; Ronnholm, G.; Kalkkinen, N.; Quinn, B. M. Solvent-Dependent Stability of Monolayer-Protected Au_{38} Clusters. *J. Phys. Chem. Lett.* **2009**, *1*, 32–37.
- (67) Jupally, V. R.; Dharmaratne, A. C.; Crasto, D.; Huckaba, A. J.; Kumara, C.; Nimmala, P. R.; Kothalawala, N.; Delcamp, J. H.; Dass, A. $\text{Au}_{137}(\text{SR})_{56}$ Nanomolecules: Composition, Optical Spectroscopy, Electrochemistry and Electrocatalytic Reduction of CO_2 . *Chem. Commun.* **2014**, *50*, 9895–9898.
- (68) Zhang, G.; Musgrave, C. B. Comparison of DFT Methods for Molecular Orbital Eigenvalue Calculations. *J. Phys. Chem. A* **2007**, *111*, 1554–1561.
- (69) Holcombe, T. W.; Yum, J.-H.; Yoon, J.; Gao, P.; Marszalek, M.; Censo, D. D.; Rakstys, K.; Nazeeruddin, M. K.; Graetzel, M. A Structural Study of DPP-based Sensitizers for DSC Applications. *Chem. Commun.* **2012**, *48*, 10724–10726.
- (70) Qian, H.; Zhu, M.; Andersen, U. N.; Jin, R. Facile, Large-Scale Synthesis of Dodecanethiol-Stabilized Au_{38} Clusters. *J. Phys. Chem. A* **2009**, *113*, 4281–4284.
- (71) Dharmaratne, A. C.; Krick, T.; Dass, A. Nanocluster Size Evolution Studied by Mass Spectrometry in Room Temperature $\text{Au}_{25}(\text{SR})_{18}$ Synthesis. *J. Am. Chem. Soc.* **2009**, *131*, 13604–13605.
- (72) Dass, A.; Holt, K.; Parker, J. F.; Feldberg, S. W.; Murray, R. W. Mass Spectrometrically Detected Statistical Aspects of Ligand Populations in Mixed Monolayer $\text{Au}_{25}\text{L}_{18}$ Nanoparticles. *J. Phys. Chem. C* **2008**, *112*, 20276–20283.
- (73) Angel, L. A.; Majors, L. T.; Dharmaratne, A. C.; Dass, A. Ion Mobility Mass Spectrometry of $\text{Au}_{25}(\text{SCH}_2\text{CH}_2\text{Ph})_{18}$ Nanoclusters. *ACS Nano* **2010**, *4*, 4691–4700.